Atmospheric Environment 351 (2025) 121176

Contents lists available at ScienceDirect

Atmospheric Environment

journal homepage: www.elsevier.com/locate/atmosenv

Tracking NO_2 and CO pollution hotspots at provincial scale in China with TROPOMI observations and image segmentation method

Mingyu Zeng [a], Minghui Tao [a,*], Rong Li [b], Pengfei Ma [c], Lijuan Zhang [c], Jun Wang [d], Lunche Wang [a], Yi Wang [a], Haijun Huang [a], Liangfu Chen [e]

[a] Hubei Key Laboratory of Regional Ecology and Environmental Change, School of Geography and Information Engineering, China University of Geosciences, Wuhan, 430074, China
[b] Faculty of Resources and Environmental Science, Hubei University, Wuhan, 430062, China
[c] Center for Satellite Applications on Ecology and Environment, Ministry of Ecology and Environment, Beijing, 100094, China
[d] Center for Global and Regional Environmental Research, The University of Lowa, Lowa, IA, 52242, USA
[e] State Key Laboratory of Remote Sensing Science, Aerospace Information Research Institute, Chinese Academy of Sciences, Beijing, 100101, China

HIGHLIGHTS

- Provincial-scale pollution hotspots were identified based on image segmentation.
- First identification of oversampled CO pollution hotspots using image segmentation.
- Identify major emission sectors for pollution hotspots in each province.

ARTICLE INFO

Keywords:
NO_2
CO
Provincial-scale
Image segmentation
Emission source

ABSTRACT

Satellite measurements of short-lived gaseous pollutants such as nitrogen dioxide (NO_2) and carbon monoxide (CO) provide an unprecedented opportunity to infer global distribution of their emission sources. However, the great differences in the magnitude of anthropogenic emissions have hampered the identification of pollution sources with satellite observations. In this study, we identified NO_2 and CO pollution hotspots in China with oversampled TROPOspheric Monitoring Instrument (TROPOMI) concentration data by utilizing an image segmentation method at provincial scale. We also determined the major emitting sectors associated with the pollution hotspots in each province. Based on NO_2 pollution hotspots, we can find major emission sources, such as ports, airports, industrial and urban areas. In the hotspots of most provinces, Steel plant, Coke plant, and Power plant were identified as the main NO_x emission sources. CO pollution hotspots were closely linked to Steel plant, with additional contributions from Coke plant, Chemical industry, and Non-ferrous metal smelting in certain provinces. The pollution hotspots and their corresponding concentrations yielded a relatively strong correlation with Multi-resolution Emission Inventory for China (MEIC) (For NO_2, the R^2 was 0.937 in provinces with small land area and 0.654 in others, while for CO, the R^2 was 0.849 and 0.659, respectively). Our results can provide an observational constraint on the spatial locations of NO_x and CO emission sources for emission inventories.

1. Introduction

Nitrogen oxides ($NO_x = NO + NO_2$) and carbon monoxide (CO) are two key air pollutants that play important roles in air quality, ecosystems, climate change, and are detrimental to public health (Daniel and Solomon, 1998; Jion et al., 2023; Richter et al., 2005). Anthropogenic NO_x emissions are mainly released from combustion in the energy sectors and exhaust emissions from mobile sources (Bhanarkar et al., 2005). CO is emitted into the atmosphere primarily by incomplete combustion of fossil fuels and biomass (Hoesly et al., 2018). These two gases are mainly concentrated in urban areas with frequent human activities (Chen et al., 2023; Crippa et al., 2018). The bottom-up emission

* Corresponding author. NO. 388, Lumo Road, Hongshan District, Wuhan 430074, China.
E-mail address: taomh@cug.edu.cn (M. Tao).

https://doi.org/10.1016/j.atmosenv.2025.121176
Received 23 December 2024; Received in revised form 11 March 2025; Accepted 14 March 2025
Available online 14 March 2025

inventories of NO_x and CO traditionally allocate total emissions to a grid by applying spatial proxies, such as population density and road networks. However, due to the mismatch between the actual emission locations and the spatial proxies, biases occur in grid emissions (Hogue et al., 2016). Therefore, accurate information on the locations of NO_x and CO emission sources is crucial for formulating pollution control strategies, as well as for updating and validating emission inventories.

Due to the relatively shorter atmospheric lifetimes of NO_x (from hours to a day) and CO (from days to months) compared to carbon dioxide (CO_2) (Beirle et al., 2011; Holloway et al., 2000), their concentrations are distributed primarily near local emission sources, making them useful for studying their sources. Satellite measurements provide valuable spatiotemporal patterns and concentrations of NO_2 and CO on a global scale (Duncan et al., 2014; Jamali et al., 2020; Martin, 2008), enabling the observation of distinct pollution hotspots in monthly or annual average images. Furthermore, pronounced pollution plumes were evident in daily images from high-resolution sensors, such as the TROPOspheric Monitoring Instrument (TROPOMI) (Finch et al., 2022; Tian et al., 2022; Varon et al., 2024). Recently, machine learning has been effectively applied to identify pollution hotspots by fusing multi-source measurements data and analyzing plume features in large datasets (Finch et al., 2022; Fu et al., 2023; Schuit et al., 2023). Furthermore, the wind rotation method proposed by Pommier et al. (2013) provides a well-established approach for source localization, integrating multiple observations while preserving the structure of emission plumes. However, its applicability is limited in areas with multiple surrounding sources. Biases in the assumed rotation reference points and interference from nearby source signals can erroneously amplify the studied source signal, leading to localization errors (Pommier, 2023).

Image segmentation methods are widely used in image processing and recognition, effectively distinguishing between the foreground and background. At the national scale, this method has been used to identify major NO_2 pollution hotspots in central and eastern China (Wang et al., 2022). However, differences in pollutant concentration distributions across spatial scales affect hotspot identification. The segmentation criterion for the national scale may omit hotspots with lower concentrations at the national level, but have significant impacts at finer-scale regions. In addition, industrial structures and emissions vary considerably across Chinese provinces (Cheng et al., 2018; Sheng et al., 2024; Wang et al., 2021; Xue et al., 2022), with air pollution levels generally higher in the industrially dense eastern coastal and northern provinces than in western and inland regions. Therefore, a uniform segmentation criterion is inadequate for characterizing provincial pollution hotspot distributions accurately. Given that provinces serve as key administrative entities for pollution control, the provincial scale is a suitable spatial scale to identify pollution hotspots and develop targeted mitigation strategies. While image segmentation has been successfully applied to identify NO_2 pollution hotspots, its application to CO hotspot identification remains unexplored.

In this study, NO_2 and CO hotspots were identified at the provincial scale using image segmentation methods, highlighting regional variations. Section 2 introduces the study area, the satellite products and the methodologies we used. Section 3.1 describes the characteristics of the provincial background values obtained from the image segmentation process. Section 3.2 presents the results of NO_2 and CO pollution hotspots identification, while Section 3.3 evaluates the link between pollution hotspots concentrations and emissions. The primary sector types for the pollution hotspots are analyzed in Section 3.4. Conclusions are provided in Section 4.

2. Data and methods

2.1. Study area

The study area consists of 32 provinces in China (Fig. 1a), with each province analyzed individually. Hong Kong and Macau are excluded from this study due to their small land area, which makes them unsuitable for the methods applied in this research.

2.2. Satellite data

TROPOMI, launched in October 2017 aboard the Sentinel 5-Precursor satellite, provides observations of various critical atmospheric pollutants, including NO_2 and CO. TROPOMI provides measurements of NO_2 tropospheric vertical column densities (TVCDs) through its visible channel and CO total column densities (TCDs) through its shortwave infrared channel. TROPOMI has an unprecedented spatial resolution of up to 3.5×7 km^2 for NO_2 at nadir and 7×7 km^2 for CO. Since August 6, 2019, the resolution has been further enhanced to 3.5×5.5 km^2 and 7×5.5 km^2, respectively. In addition, TROPOMI has a high signal-to-noise ratio that enables daily observations of NO_2 and CO pollution in urban and industrial areas through single orbit overpasses (Borsdorff et al., 2018; van Geffen et al., 2020), and reliable statistical results for both annual and monthly data can be obtained. For this study, the daily NO_2 TVCDs and CO TCDs from January to December 2019 are TROPOMI Level 2 offline timeliness products, accessible through the ESA Copernicus Open Access Hub and the NASA Earth Data Portal.

TROPOMI NO_2 and CO were oversampled to $0.01^\circ \times 0.01^\circ$ spatial resolution on a monthly basis using the physics-based oversampling approach proposed by Sun et al. (2018), as shown in Fig. 2. This method is developed to represent each satellite observation as a sensitivity distribution on the ground, significantly improving the visualization of

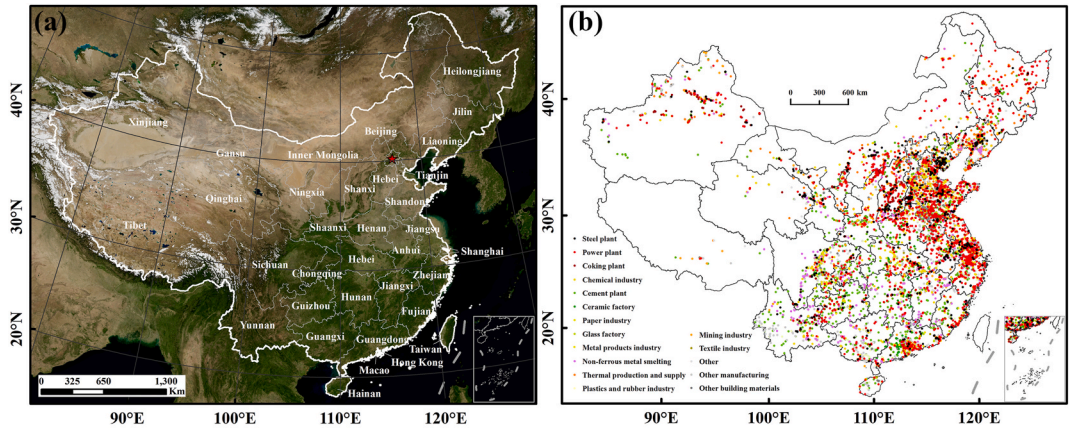

Fig. 1. Study Area (a): 32 Provinces of China (Excluding Hong Kong and Macau); (b): Industry sectors and spatial distribution of the 2019 National Directory of Key Pollutant Emission Units (the data of Hong Kong, Macau, and Taiwan are not available).

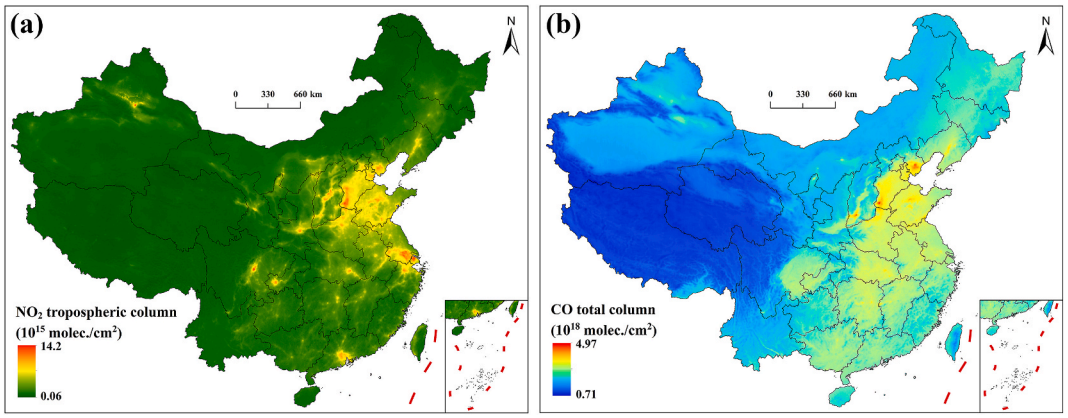

Fig. 2. The annual-averaged oversampled NO_2 tropospheric column (a) and CO total column (b) over the study area for 2019.

trace gas distribution and local gradients within a short temporal window. Therein, the NO_2 and CO pixels were filtered based on quality assurance values above 0.75 and 0.5, and cloud fraction values below 0.5 and 0.3, respectively.

2.3. Supplementary data

Power plant data were obtained from the Global Power Plant Database of World Resources Institute (WRI, https://datasets.wri.org/dataset/globalpowerplantdatabase, Version 1.3.0). Data from three types of power plants with higher pollutant emissions were selected: coal, gas, and oil. Steel plant data were sourced from the Global Steel Plant Tracker of Global Energy Monitor (GEM, https://globalenergymonitor.org/projects/global-steel-plant-tracker/), with only those operational in 2019 included. The key parameter, nominal crude steel capacity, represents the production capacity of each steel plant.

The Multi-resolution Emission Inventory for China (MEIC, http://meicmodel.org.cn) provides anthropogenic emission data for 2019 at a spatial resolution of $0.25^\circ \times 0.25^\circ$ (Geng et al., 2024; Li et al., 2017). MEIC contains NO_x and CO emissions from five anthropogenic sectors (i.e., agriculture, power plant, industry, residential, and transportation). Here, we did not consider the agriculture sector due to its relatively low emissions and it is too diffuse to appear as hotspots in the satellite data.

We obtained the 2019 National Directory of Key Pollutant Emission Units (https://data.epmap.org/product/keypollutions) and conducted data preprocessing. In particular, industrial sectors that rely on extensive fuel combustion for high-temperature processes and make substantial contributions to air pollutants emissions were identified as major stationary combustion sectors. Table S1 listed the sectors (including major stationary combustion sectors) and corresponding numbers from the list used in this study, while their spatial distribution was shown in Fig. 1b.

2.4. Image segmentation method

Image segmentation is an important technique in image processing. It partitions an image into regions with similar features, facilitating the extraction of regions of interest (ROI). Thresholding methods, low computational cost methods for image segmentation, are useful for eliminating background noise (Haralick and Shapiro, 1985). These methods include global and local methods, with the former segmenting an image based on information obtained globally, while the latter considers the local properties of pixels and their neighborhoods.

2.4.1. Fractal model

The fractal model is a global threshold segmentation method that is widely used for determining geochemical element thresholds (Shen, 2011) and analyzing background values of atmospheric pollutants (Chen et al., 2012, 2018). This model, which has been shown to obtain higher global background values for NO_2 TVCDs compared to the Otsu method, can be used to evaluate the monthly background values of NO_2 columns (Wang et al., 2022). This method analyzes and describes the fractal characteristics of cumulative density distributions of objects, wherein the number of objects exceeding a certain scale is characterized by a power-law relationship with the size scale of the objects. Based on this, Shen (2011) proposed the fractal summation model as shown in Eq. (1):

$$N(r) = \sum_{i=1,\ x_i \geq r}^{n} x_i = Cr^{-D} \tag{1}$$

Where $N(r)$ represents the total number of objects for which $x_i \geq r$, corresponding to the number of objects with a characteristic scale greater than or equal to r, with $\min_{1\leq i\leq n} x_i \leq r \leq \max_{1\leq i\leq n} x_i$. D is the fractal dimension, and C is the constant of proportionality.

The main idea is to determine two appropriate threshold points (r_1 and r_2) that minimize the sum of squared differences between the original data and the fitted values within the three intervals. In this study, a piecewise linear model was fitted using the least squares method based on Eq. (1) and the concentration distribution of each province to automatically determine these thresholds, with the first threshold point serving as the provincial background concentration for background elimination.

2.4.2. Adaptive threshold method

Pollution sources and causes in China are complex due to factors such as industrial activities, urbanization, and transportation, leading to a variable distribution of emission sources across different city clusters and cities. Therefore, it is essential not only to determine an appropriate global threshold but also to establish more refined local threshold to avoid misclassifying vague boundaries as background. The adaptive threshold method, a typical local thresholding approach based on the foreground-background contrast, dynamically calculates every point of image with sliding window image processing (Sezgin and Sankur, 2004). A Gaussian window was used to extract hotspot ROI by weighting neighboring pixels after eliminating the global background in this study. The window size, which is a key factor influencing threshold determination, was adjusted based on the specific characteristics of each region. It was generally set smaller in industrially developed provinces with concentrated emissions to capture finer spatial variations. Due to the more uniform distribution and lower spatial variability of CO compared to NO_2, a larger window was typically required to capture broader spatial changes and minimize noise.

2.4.3. Hotspot grid index construction

Following the local threshold segmentation, the results were binarized to calculate the frequency of hotspot ROI within each $0.01^\circ \times 0.01^\circ$

(~1 km × 1 km) grid over a 12-month period. In the binarization process, grids within hotspot ROI, termed hotspot grids, were set to 1, while others were set to 0. This frequency served as an indicator of air pollutants hotspot grids and was referred to as the Hotspot Grid Index (HGI), as shown in Eq. (2). Higher HGI indicated a higher frequency of the grid falling within the hotspot ROI over the 12-month period but did not directly reflect emission intensity. The HGI was constructed for each province within the study area.

$$HGI = \sum_{1}^{m} T_i \tag{2}$$

Where m is the total number of months in the study period, T_i indicates the binarized value of the grid for month i, with a value of either 1 or 0.

2.5. Term frequency-inverse document frequency (TF-IDF) method

TF-IDF is a widely used method in natural language processing (NLP) for evaluating the importance of a term in a document set or corpus. TF-IDF is calculated as TF × IDF, where TF is the frequency of a term in a given document and IDF measures the importance of a term by down-weighting frequent terms and upweighting rare ones. As such, a high TF-IDF weight is achieved when a term appears frequently in a specific document but rarely across the entire document set. This method is widely applied in information retrieval (Nguyen, 2013; Salton and Buckley, 1988) and text-based recommender systems (Beel et al., 2016). In our study, the industry sectors from the 2019 National Directory of Key Pollutant Emission Units were treated as "terms". The TF-IDF method was used to identify the primary industry sectors contributing to pollution in the hotspot grids of different pollutants. The specific formula is given as shown in Eq. (3):

$$TFIDF_{ij} = TF_{ij} \times IDF_j = \frac{n_{i,j}}{\sum_k n_{k,i}} \times \log \frac{N}{DF_j} \tag{3}$$

Where $n_{i,j}$ is the number of key pollutant-emitting units of industry type j found in hotspot ROI i, $\sum_k n_{k,i}$ represents the total number of all key pollutant-emitting units in area i. N is the total number of key pollutant-emitting units in study area, and DF_j is the total number of key pollutant emission units of industry type j in study area.

3. Results and discussions

3.1. Characteristics of provincial background values

The background values of NO_2 and CO in most provinces, derived from the Fractal method, fall between the first and third quartiles of the oversampled data, closer to the third quartile (Fig. S1). To understand the differences between each province's background values and the national background values, we also obtained the national background values for NO_2 and CO using the same method. We found that the national-scale background values for both NO_2 and CO were significantly higher than the third quartile of their concentrations, which was likely primarily driven by provinces with higher background values.

As shown in Fig. 3a, In Shanghai, Shandong, Hebei, Beijing, Tianjin, and Henan, the monthly background values of NO_2 TVCDs exceeded the national level (shown by the black line) for more than five months, with these provinces primarily located in northern China (Fig. 3c). Meanwhile, 14 provinces had the monthly background values of CO TCDs exceeding the national level (shown by the black line) for over five months (Fig. 3b), mainly distributed in eastern and southern China (Fig. 3d). These provinces can be considered as having a considerable contribution to China's air pollution throughout the year. Notably, Guangdong and Guangxi showed the highest background values of CO TCDs in March and April, likely influenced by biomass combustion in Southeast Asia (Deng et al., 2008; Huang et al., 2013). Although some provinces exceeded the national background values for more than five months, the majority (18 out of 32) did not, underscoring the necessity

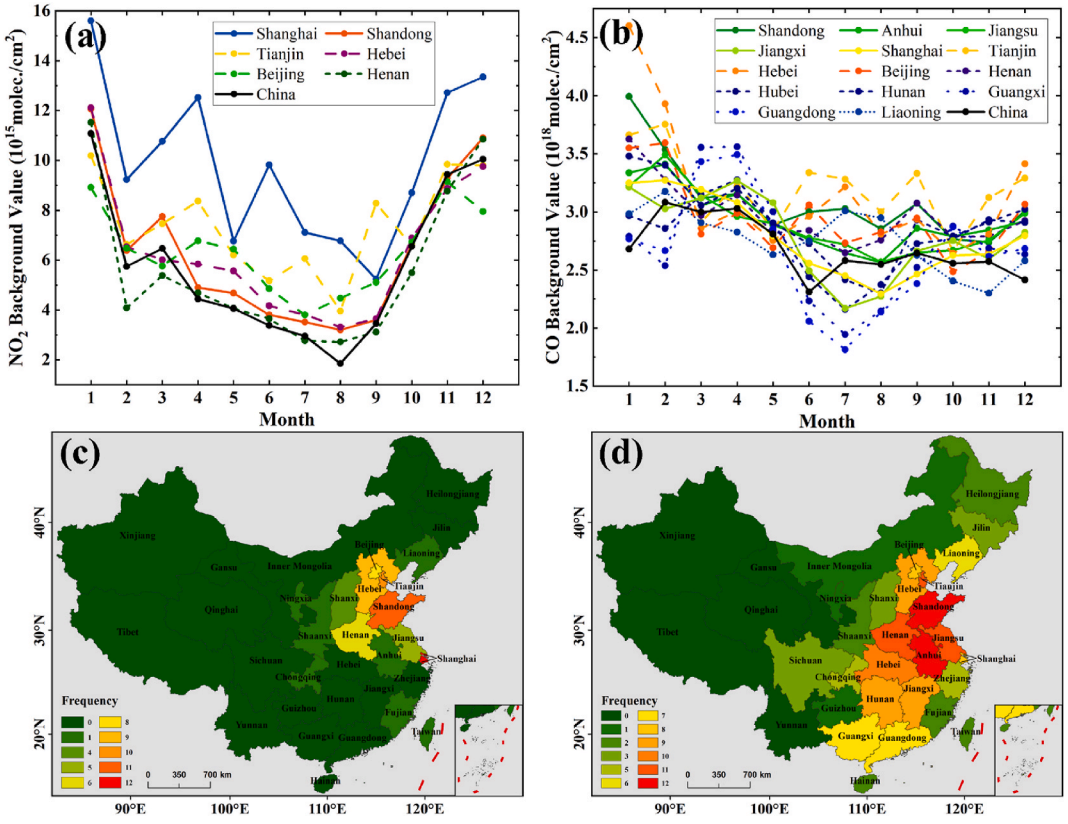

Fig. 3. Provinces with more than 5 months exceeding the national background values (black line) over 12 months: (a, c) NO_2; (b, d) CO.

of using provincial thresholds in research. Therefore, this study focused on the provincial scale to ensure consistent analysis.

3.2. Identification of hotspot grids

To improve the reliability of hotspot grids, we extracted hotspot grids with HGI ≥5, indicating they were identified as hotspots for at least five months, as shown in Fig. 4 for NO_2 and Fig. 6 for CO.

3.2.1. NO_2

The provincial-scale NO_2 hotspot grids extracted by our study reflected the main NO_x emission regions and their distribution across provinces (Fig. 4a). The localized hotspot grids for Shaanxi, Hubei, Anhui, Jiangsu, Guangxi, and Xinjiang provinces were illustrated in Fig. 4b–g. These hotspot grids were found to capture the majority of steel plants, power plants, and other major stationary combustion sources (listed in Table S1) in each province. In addition, several large lakes in the Tibet region were identified as NO_2 hotspots (Fig. 4h). Kong et al. (2023) attributed this to the unique and rapidly changing environment on the plateau, which affected lake microbial activities, leading to high nitric oxide (NO, a precursor to NO_2) emissions from remote lakes.

Taking Guangdong province as an example, we demonstrated the capability of hotspot grids to extract NO_2 pollution hotspots (Fig. 5). Hotspot grids in Guangdong were found not only in the Pearl River Delta (PRD) region but also in the eastern, western, and northern regions of the province, where NO_2 concentrations were lower than in the PRD. These hotspot grids encompassed a variety of sources, including ports (e.g., Western port area of Shenzhen Port, Yantian Port and Zhuhai Port, SZPW, YTP & ZHP) and airports (e.g., Guangzhou Baiyun International Airport, GBIA), as well as steel plants, cement plants, power plants, industrial parks, and urban areas. The ceramic industry in Guangdong plays a pivotal role nationally, as shown in the figure, which highlighted the hotspot grids of two major ceramic factories in Yunfu and Zhaoqing cities. In addition to the prominent hotspots, small hotspots also provided valuable information. For example, cement plants were identified based on small hotspots (marked with blue triangles).

3.2.2. CO

Because CO has a moderate lifetime, which is longer than that of NO_2, it mixes more easily with the atmosphere. As a result, CO concentrations are more uniformly distributed on an annual basis compared to NO_2, making it more challenging to achieve high HGI values at the national-scale for CO. Nonetheless, provincial-scale hotspot grids effectively identified the major CO pollution sources in each province

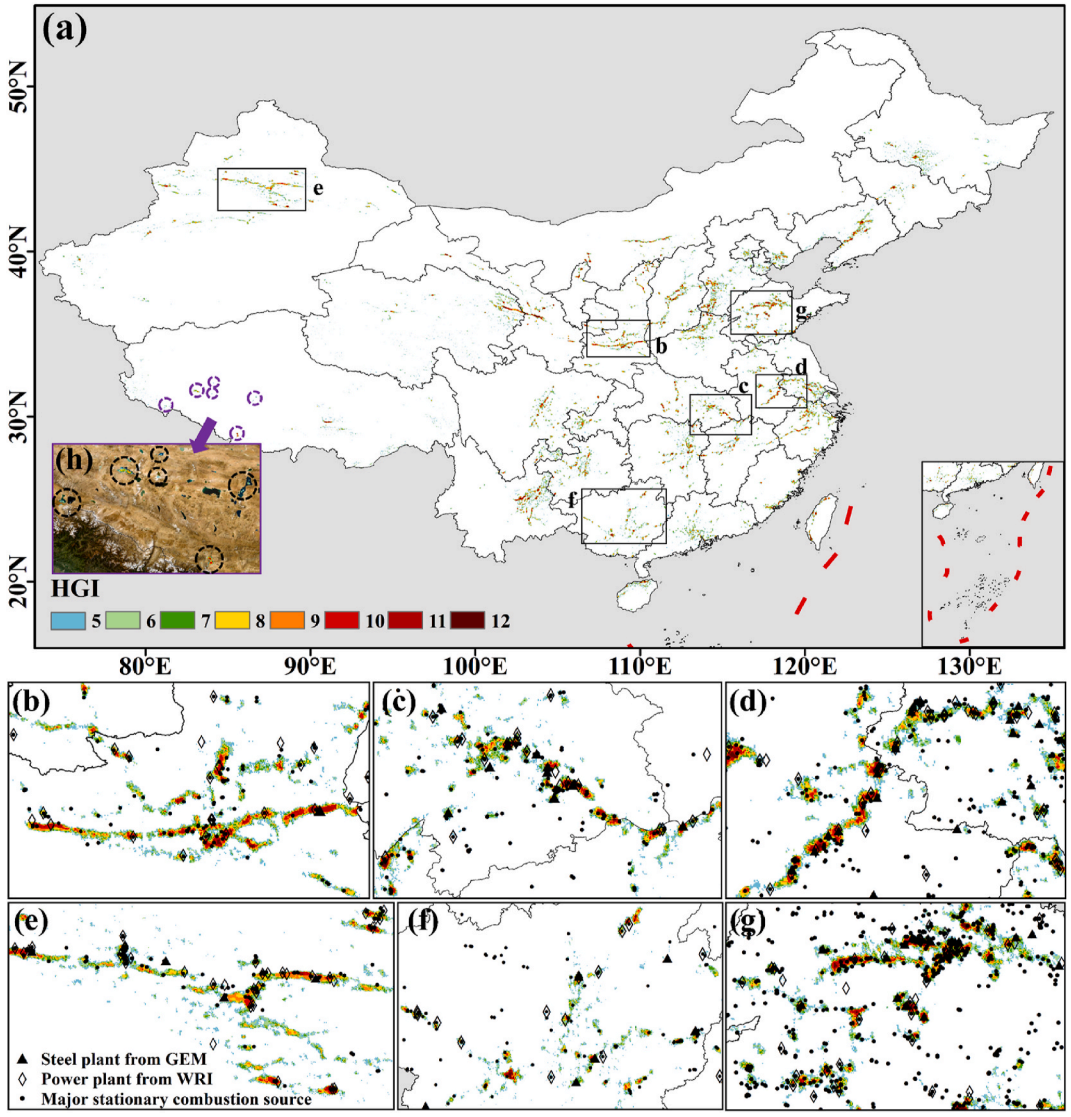

Fig. 4. Provincial-scale hotspot grids for NO_2 in the study domain (a), and localized results for HGI ≥5 overlaid with steel plants, power plants and major stationary combustion sources in (b)–(g); (h) represents NO_2 hotspot grids in some lakes of Tibet.

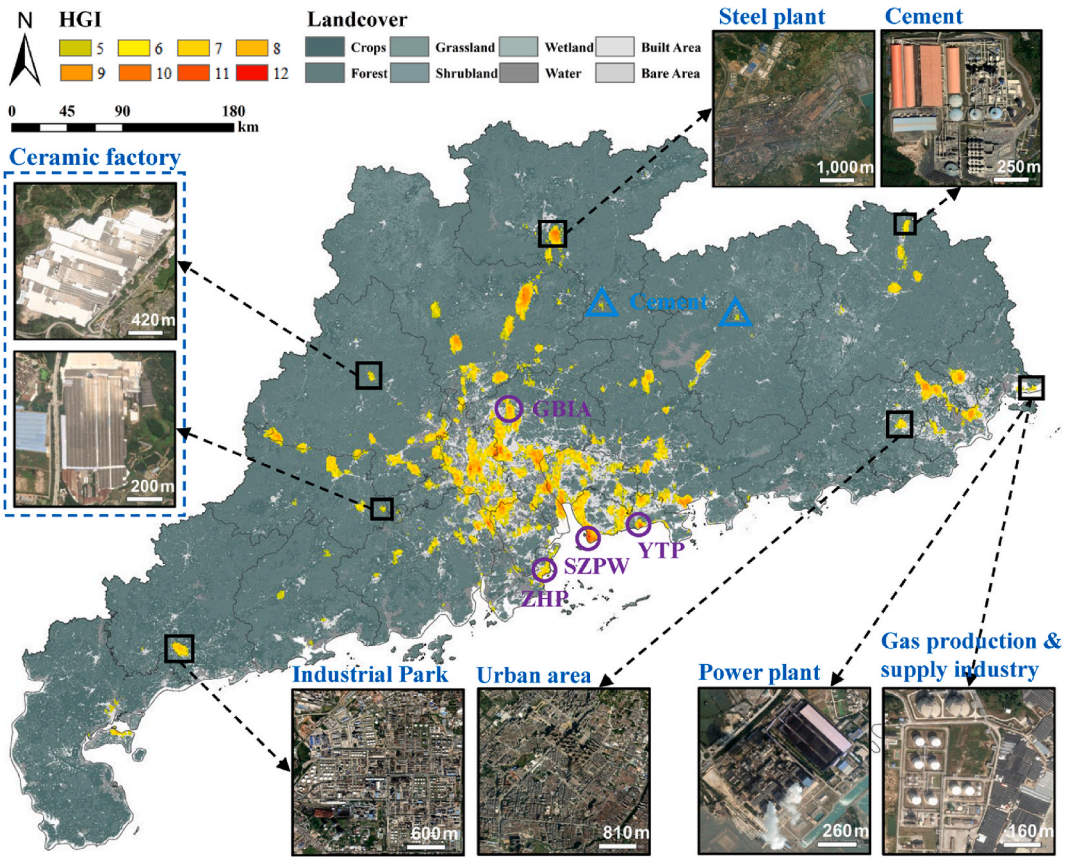

Fig. 5. Provincial-scale hotspot grids for NO_2 in Guangdong. The snapshots show high-resolution images of major types of NO_2 pollution sources.

(Fig. 6a). Since CO mainly arises from incomplete combustion, areas with high HGI values showed a spatial distribution closely aligned with regions dominated by heavy industry, particularly the steel sector. The localized hotspots in Shaanxi, Hebei, Shandong, Anhui, Jiangsu, and Liaoning provinces were shown in Fig. 6b–f. It was found that their high HGI values were closely associated with steel plants, especially those with a crude steel production capacity exceeding 3200 thousand tonnes per annum (ttpa). Due to topographical factors and the lifetime characteristics of CO, regions with limited dispersion, such as valleys and lakes, exhibited numerous high HGI values. In southern Yunnan (Fig. 6h), this phenomenon could be primarily attributed to biomass burning originating from Southeast Asia (Yin et al., 2021). In contrast, in eastern Qinghai (Fig. 6g), it was likely associated with localized emission sources, such as Xining Special Steel and urban areas. Accurately distinguishing whether CO hotspots originate from local emissions or result from the accumulation of transported pollutants is challenging in complex terrain.

Using Tianjin, Tangshan, and Handan as examples, the capability of hotspot grids to identify CO pollution hotspots was demonstrated (Fig. 7). These three cities, located within the Beijing-Tianjin-Hebei (BTH) urban cluster, are representative heavy industrial cities in China. Tangshan, in particular, is the largest steel production base in the country, with a crude steel production of 136.89 million tons in 2019 (Tangshan Municipal Bureau of Statistics, https://www.tangshan.gov.cn/zhuzhan/zw_tongjijutjsj/20200605/948709.html). By comparing the CO oversampled concentration map, the hotspot grids identified pollution hotspots from heavily polluted areas. In addition to the steel plants already existing in GEM, the Tianjin Tianzhong Giant Heavy Industry Steel plant (TGHIS) was identified. Beyond steel plants, the Qian'an Jiujiang Coke plant (QJC) in Tangshan, the Lushun Coke plant (LSC) and the Jinyu Taihang Cement plant (JTC) in Handan were also identified.

While provincial-scale hotspot grids can identify urban pollution hotspots, their clustering in heavily polluted areas suggests that current thresholds may miss local variations. This highlights the potential of finer-scale (e.g., urban-scale) background concentrations to further refine hotspot boundaries and reveal additional pollution sources. It is important to note that satellite tracking of emission sources is constrained by inherent limitations. In addition to coarse resolution, which may fail to capture small sources, emission intensity and the type of gas species also play crucial roles. Weaker emissions may not form distinct hotspots, and the atmospheric lifetime and transmission properties of NO_2 and CO further influence the detectability of these sources.

By overlaying the provincial hotspot grids for NO_2 and CO, overlapping areas indicate common emission sources (Fig. 8). Since both gases share common combustion sources, and considering that NO_2 has a shorter atmospheric lifetime and is less influenced by topography in monthly averaged data than CO, this distinction may provide insight into whether CO hotspots in valleys result from topographically induced accumulation or local emissions.

3.3. *Evaluation of hotspot grids using MEIC*

We conducted a linear regression analysis between the MEIC emission data and the concentrations corresponding to the hotspot grids to evaluate the extraction of the hotspot grids. According to the clustering feature in scatter plots representing annual average gas concentrations and annual total emissions from MEIC corresponding to the hotspot grids in different provinces (Fig. S2), we found that these data points can be divided into two groups (Fig. 9).

Group 1 (rectangle) includes Shanghai, Tianjin, and Beijing, which displayed relatively high average concentration values but low total emissions. As provincial-level municipalities, Shanghai, Tianjin, and Beijing are characterized by high population densities and intense urban

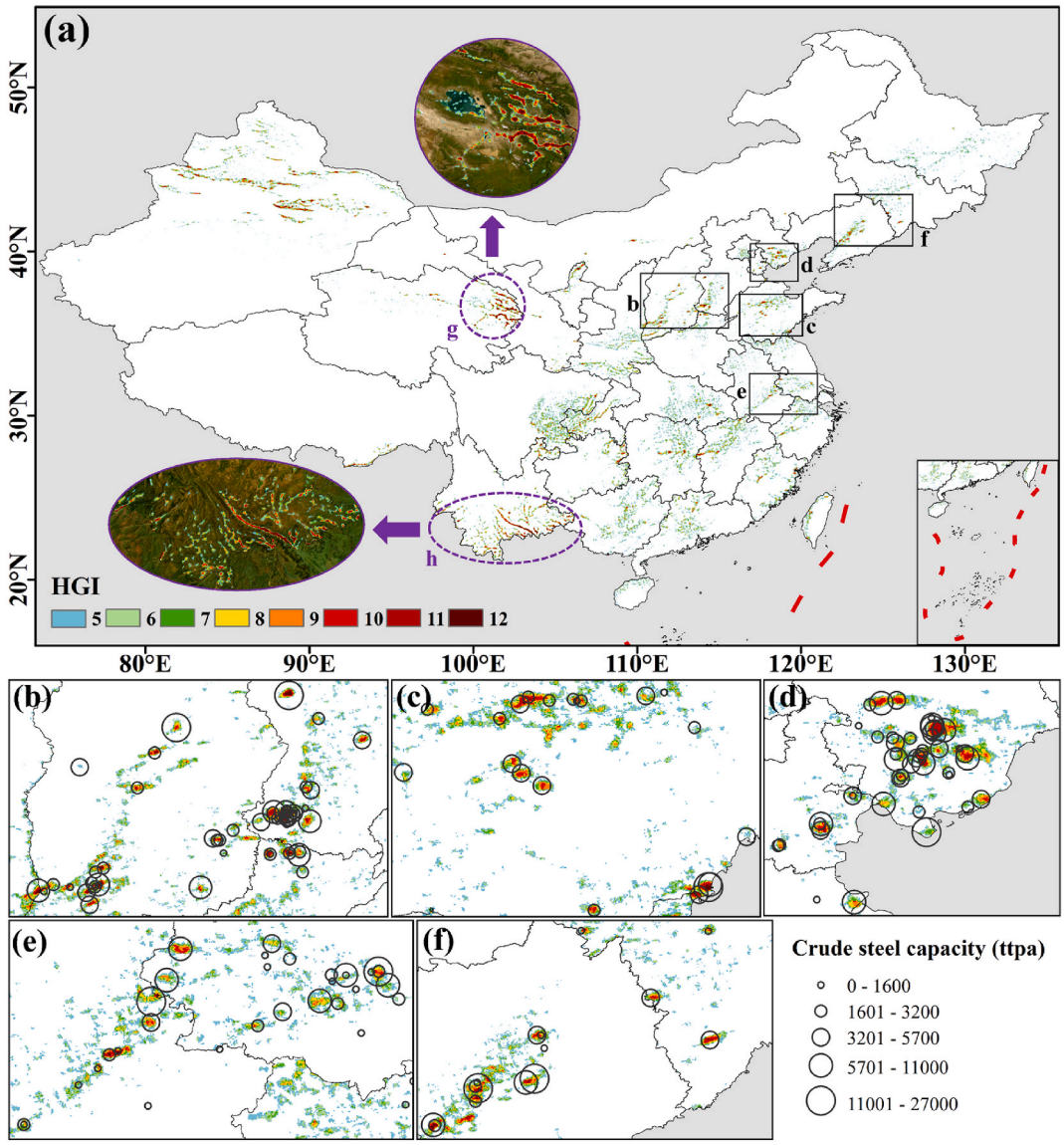

Fig. 6. Provincial-scale hotspot grids for CO in the study domain (a), and localized results for HGI ≥5 overlaid with steel plants in (b)–(f); (g) and (h) show hotspot grids influenced by topography.

activities, which contribute to high background concentrations (Fig. 3). In addition, due to their small land areas and the coarse resolution (0.25° × 0.25°) of the MEIC inventory, hotspots are concentrated within a limited number of emission grids. The other provinces with larger land areas and more spatially dispersed hotspots formed Group 2 (circle). Following the grouping, the R^2 values between MEIC emissions and NO_2 or CO concentrations significantly increased——from 0.272 to 0.937 and 0.654 for NO_2, and from 0.412 to 0.849 and 0.659 for CO. It should be noted that NO_2 and CO concentrations were extracted at HGI ≥5 and HGI ≥4, respectively, yielding the strongest correlations. The hotspot grids highlight key pollution areas, emphasizing the relationship between emissions and concentrations when compared to the whole province analysis (Fig. S3). The hotspot grids captured local variations in emissions and pollutant concentrations, and demonstrated their capability to accurately identify pollution sources and assess local emissions.

3.4. TF-IDF analysis

To determine the dominant sources of gas pollution in various HGI, the TF-IDF weights for each industry type were calculated based on the 2019 National Directory of Key Pollutant Emission Units in study area. When HGI = 12, Steel plant, Power plant, and Coking plant were the major emission sources in NO_2 hotspot grids, indicating their emissions were the main drivers for these grids being identified as hotspots for all 12 months (Table 1). High TF-IDF weights for Power plant were observed in various HGI values. Steel plant and Coking plant displayed a clear upward trend in TF-IDF weights as HGI increased. Thermal production and supply, Ceramic factory and Non-ferrous metal smelting also showed modest increases in TF-IDF weights with rising HGI, while Cement plant maintained relatively high TF-IDF weights across various HGI values, highlighting their important contributors to NO_2 hotspot grids. It was further observed that at lower HGI, Other manufacturing and Chemical industry were the major industry types.

In contrast to the high TF-IDF weights observed for multiple industry types in the NO_2 hotspot grids at HGI = 12, Steel plant exhibited particularly prominent TF-IDF weight in the CO hotspot grids, increasing with HGI and establishing them as the dominant emission source (Table 2). With the increase of HGI, the TF-IDF weights for Coking plant similarly showed a notable increase. Non-ferrous metal smelting, Chemical industry, Power plant, and Cement plant also exhibited high TF-IDF weights in different HGI, indicating their

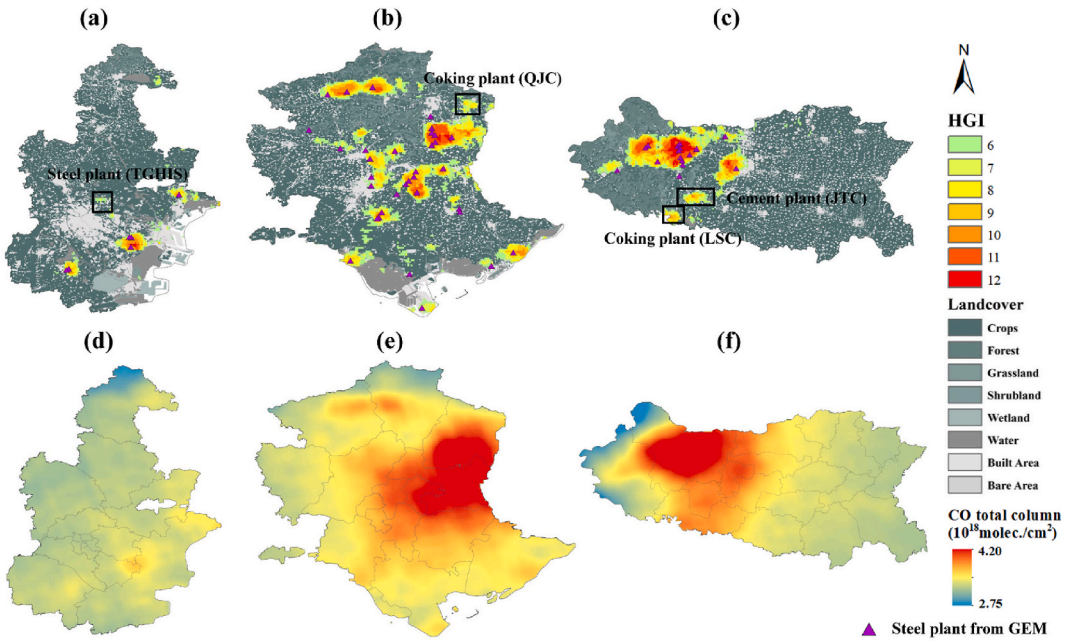

Fig. 7. Provincial-scale CO hotspot grids and annual-averaged oversampled CO total column for Tianjin (a, d), Tangshan (b, e), and Handan (c, f).

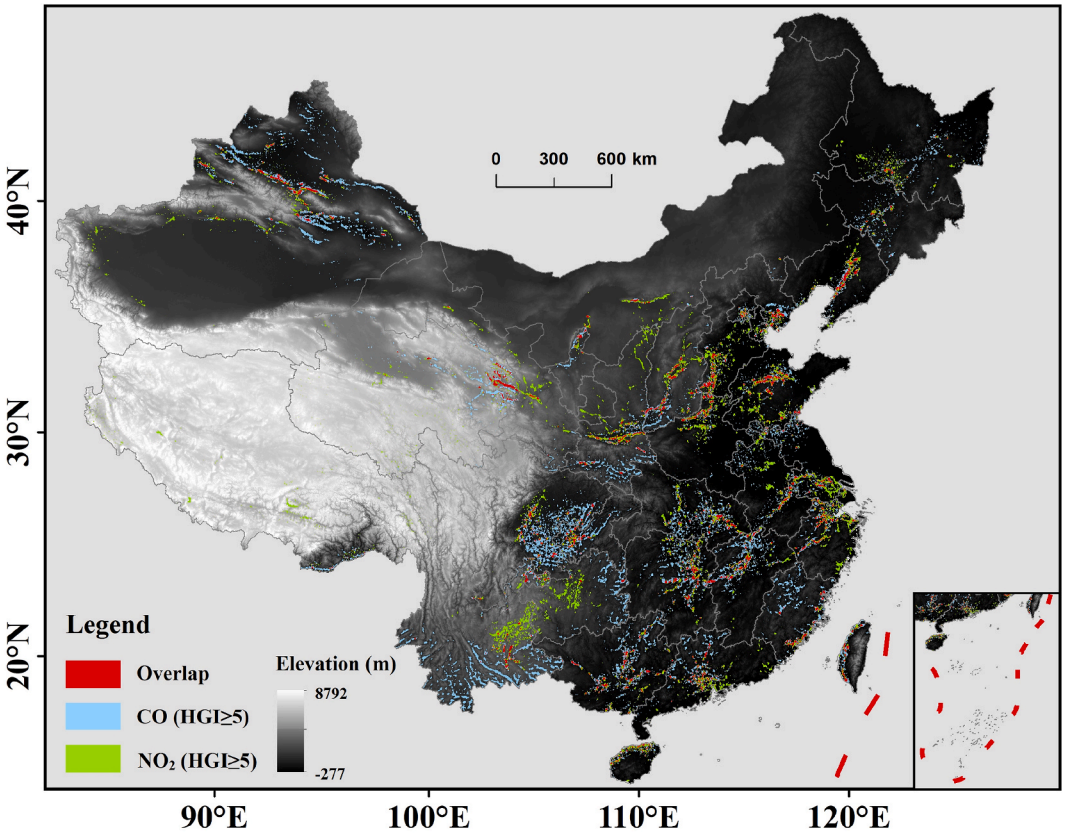

Fig. 8. Overlap of provincial-scale hotspot grids for CO and NO_2 with HGI ≥5.

contributions to CO emissions. In contrast, Thermal production and supply, as well as Ceramic factory, were mainly linked to grids with lower HGI, reflecting their limited contribution to CO hotspots.

Tables 3 and 4 present the two major stationary combustion source types of NO_2 and CO hotspot grids at different HGI, with the highest TF-IDF weights in each province. The types that appear at least three times across different HGI results bolded at their last occurrence. Steel plant and Power plant emerged as the predominant emission sources for both NO_x and CO in most provinces. In northern China, the strong demand for heating during winter made Thermal production and supply sectors major NO_x emission sources, particularly in regions such as Beijing, Heilongjiang, and Liaoning. In many southern provinces, we found

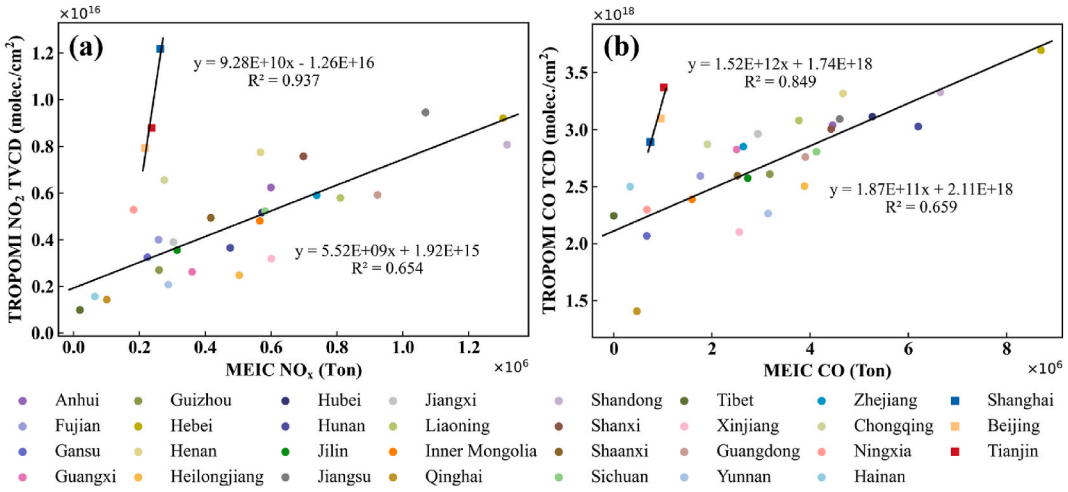

Fig. 9. Linear regression between NO_2 column concentrations corresponding to HGI ≥5 and MEIC emissions (a), and between CO column concentrations corresponding to HGI ≥4 and MEIC emissions (b) in two regions of the study area (excluding Taiwan) during 2019.

Table 1
TF-IDF weights of sectors in different HGI of NO_2.

Sector	HGI≥1	HGI≥2	HGI≥3	HGI≥4	HGI≥5	HGI≥6	HGI≥7	HGI≥8	HGI≥9	HGI≥10	HGI≥11	HGI=12
Steel plant	0.063	0.068	0.074	0.078	0.083	0.088	0.096	0.110	0.134	0.142	0.162	0.155
Power plant	0.121	0.121	0.121	0.120	0.119	0.121	0.120	0.126	0.130	0.126	0.123	0.135
Coking plant	0.047	0.051	0.056	0.062	0.067	0.072	0.079	0.092	0.099	0.111	0.115	0.125
Thermal production and supply	0.076	0.076	0.076	0.075	0.075	0.076	0.078	0.080	0.088	0.080	0.083	0.123
Other manufacturing	0.139	0.139	0.139	0.136	0.135	0.130	0.125	0.110	0.103	0.090	0.084	0.095
Ceramic factory	0.061	0.064	0.067	0.070	0.072	0.077	0.071	0.072	0.070	0.072	0.059	0.087
Other	0.061	0.059	0.059	0.059	0.057	0.056	0.057	0.058	0.057	0.057	0.064	0.086
Chemical industry	0.115	0.115	0.116	0.114	0.116	0.112	0.114	0.114	0.100	0.097	0.091	0.071
Non-ferrous metal smelting	0.061	0.058	0.055	0.053	0.054	0.058	0.055	0.061	0.060	0.069	0.076	0.070
Cement plant	0.082	0.084	0.084	0.086	0.083	0.086	0.082	0.082	0.078	0.084	0.082	0.067
Other Building Materials	0.057	0.052	0.047	0.047	0.047	0.047	0.050	0.051	0.062	0.073	0.106	0.038
Glass factory	0.037	0.040	0.041	0.043	0.046	0.048	0.050	0.054	0.051	0.044	0.033	0.031
Metal products industry	0.049	0.049	0.048	0.047	0.046	0.045	0.047	0.042	0.035	0.037	0.025	0.027
Mining industry	0.019	0.019	0.018	0.018	0.020	0.021	0.024	0.025	0.024	0.033	0.031	0.021
Paper industry	0.043	0.041	0.037	0.034	0.030	0.026	0.024	0.018	0.012	0.010	0.010	0.011
Textile industry	0.040	0.041	0.040	0.040	0.036	0.034	0.035	0.024	0.021	0.019	0.008	0.006
Plastics and rubber industry	0.040	0.036	0.033	0.031	0.027	0.022	0.019	0.017	0.017	0.017	0.008	0.006

Ceramic factory was notable contributor to NO_x emissions. Coking plant was primarily associated with CO pollution in northern (e.g., Tianjin, Hebei, Shanxi and Inner Mongolia) and northwestern China (e.g., Shaanxi and Ningxia). The Chemical industry was a key source of CO emissions in eastern and southwestern provinces, while Non-ferrous metal smelting played a significant role in CO pollution in provinces such as Qinghai, Xinjiang, Fujian, and Shandong.

Due to the moderate lifetime of CO and the influence of atmospheric transport (Holloway et al., 2000; Pani et al., 2019), spatial inconsistencies exist between its hotspot grids and key pollutant emission units, introducing uncertainties in the TF-IDF analysis. However, as the results have effectively identified primary emission sectors, this impact is considered minor for major stationary combustion sources. While stationary sources dominate provincial NO_x and CO emissions, this does not imply that light industry lacks contribution. Additionally, non-road mobile sources, such as airports and ports, play a significant role in NO_x emissions as shown in Fig. 5.

4. Conclusions

TROPOMI, with its unprecedented spatial resolution and high signal-to-noise ratio, combined with the oversampling method, provided finer spatial information on pollution hotspots. This study applied the image segmentation method at the provincial scale and identified NO_2 and CO hotspots in each province of China (excluding Hong Kong and Macau). The results revealed that NO_2 hotspot grids effectively identified major industrial sources as well as ports, airports, and urban areas, while CO hotspot grids were shown to be closely associated with steel plants. Due

Table 2
TF-IDF weights of sectors in different HGI of CO.

Sector	HGI≥1	HGI≥2	HGI≥3	HGI≥4	HGI≥5	HGI≥6	HGI≥7	HGI≥8	HGI≥9	HGI≥10	HGI≥11	HGI=12
Steel plant	0.064	0.071	0.085	0.104	0.136	0.181	0.231	0.281	0.349	0.358	0.390	0.395
Non-ferrous metal smelting	0.060	0.061	0.060	0.064	0.071	0.076	0.082	0.082	0.089	0.103	0.118	0.140
Coking plant	0.045	0.048	0.048	0.053	0.064	0.078	0.100	0.113	0.135	0.157	0.154	0.133
Chemical industry	0.117	0.116	0.117	0.114	0.103	0.102	0.094	0.097	0.094	0.094	0.096	0.103
Power plant	0.117	0.116	0.116	0.116	0.112	0.109	0.108	0.107	0.088	0.082	0.080	0.079
Cement plant	0.081	0.078	0.077	0.077	0.076	0.078	0.070	0.062	0.061	0.067	0.064	0.075
Other Building Materials	0.064	0.066	0.064	0.063	0.065	0.071	0.083	0.094	0.104	0.128	0.102	0.061
Other	0.063	0.064	0.062	0.060	0.058	0.058	0.056	0.057	0.052	0.050	0.060	0.051
Metal products industry	0.047	0.044	0.043	0.042	0.042	0.046	0.037	0.037	0.042	0.038	0.044	0.047
Other manufacturing	0.143	0.143	0.138	0.133	0.129	0.115	0.097	0.079	0.065	0.054	0.046	0.044
Thermal production and supply	0.072	0.071	0.067	0.065	0.063	0.057	0.055	0.050	0.038	0.025	0.031	0.036
Mining industry	0.019	0.017	0.017	0.017	0.020	0.022	0.025	0.025	0.023	0.021	0.012	0.029
Glass factory	0.034	0.037	0.040	0.039	0.034	0.025	0.023	0.022	0.023	0.016	0.011	0.027
Ceramic factory	0.057	0.055	0.061	0.066	0.061	0.046	0.035	0.024	0.012	0.010	0.009	0.000
Plastics and rubber industry	0.040	0.037	0.031	0.024	0.021	0.015	0.016	0.015	0.010	0.009	0.000	0.000
Paper industry	0.046	0.046	0.045	0.043	0.039	0.036	0.032	0.022	0.017	0.003	0.000	0.000
Textile industry	0.040	0.041	0.039	0.039	0.035	0.026	0.022	0.014	0.004	0.003	0.000	0.000

Table 3
Provincial major stationary combustion source types in different NO_2 HGI based on TF-IDF.

Region	Province	NO_2 HGI							
		≥5	≥6	≥7	≥8	≥9	≥10	≥11	= 12
North China	Beijing	PP, TH	PP, TH	PP, CI	**TH,** CI	**PP**	–	–	–
	Tianjin	SP, PP	SP, CI	TH, CI	**CI,** CK	CK, **SP**	PP	**PP**	–
	Hebei	SP, PP	SP, PP	SP, CK	SP, CK	SP, GF	SP, CF	SP, CF	**CF, SP**
	Shanxi	CK, CI	CK, CI	CK, CI	CK, CI	CK, CI	CK, SP	CK, CI	**CK, CI**
	Inner Mongolia	CI, CK	CK, CI	CK, CI	CK, **CI**	CK, SP	CK, SP	CK, SP	**CK, SP**
Northeast China	Heilongjiang	PP, TH	PP, TH	TH, PP	TH, PP	TH, PP	**TH,** PP	CI, PP	CI, **PP**
	Jilin	PP, TH	PP, CI	PP, TH	PP, CI	PP, **CI**	PP, CP	**PP,** CP	–
	Liaoning	TH, SP	TH, SP	TH, SP	TH, SP	TH, SP	TH, SP	TH, **SP**	**TH,** PP
Northwest China	Shaanxi	CK, PP	CK, PP	CK, PP	CK, PP	PP, CK	CK, CF	NM, **CK**	SP, **PP**
	Gansu	PP, CI	PP, CI	PP, CI	PP, TH	PP, CI	PP, CI	PP, CI	**PP, CI**
	Qinghai	NM, CP	CP, NM	NM, SP	NM, SP	CP, NM	NM, CP	**CP,** NM	**NM, SP**
	Ningxia	CI, CK	CI, PP	CI, PP	**CI,** PP	**PP,** CP	CP, CK	CP, **CK**	**CP,** TH
	Xinjiang	CI, PP	CI, PP	CI, PP	CI, PP	CI, SP	NM, CI	**CI,** NM	**PP, NM**
Central China	Henan	CI, PP	PP, SP	SP, CI	SP, CI	SP, **CI**	SP, CP	SP, CP	**SP,** CK
	Hubei	CI, PP	CI, PP	CI, PP	CI, PP	CI, SP	SP, **CI**	SP, PP	**PP, SP**
	Hunan	PP, CF	PP, CF	PP, CF	CF, PP	**CF,** PP	**PP,** CI	SP, CI	CK, SP
East China	Shanghai	SP, CI	CP, SP	**SP**	–	–	–	–	–
	Jiangsu	CI, PP	PP, CI	PP, CI	PP, SP	SP, PP	SP, **PP**	**SP, CI**	–
	Zhejiang	CI, PP	CI, PP	CI, PP	CI, PP	CI, PP	CP, **CI**	CP, PP	**CP, PP**
	Anhui	CI, PP	PP, CI	PP, CI	PP, CP	**PP,** CI	CI, CP	GF, **CI**	CK, GF
	Fujian	PP, SP	PP, SP	SP, NM	SP, NM	SP, NM	NM, SP	**NM, SP**	–
	Jiangxi	NM, SP	SP, CI	SP, CF	SP, CI	SP, CF	SP, CF	SP, **CF**	**SP,** PP
	Shandong	PP, CI	PP, CI	PP, CI	PP, **CI**	PP, SP	PP, SP	SP, PP	**SP, PP**
South China	Guangdong	CF, CI	CF, CI	CF, CI	CF, PP	PP, **CF**	PP, SP	**PP**	–
	Guangxi	CI, PP	CI, PP	CI, CF	CF, CI	**CF,** PP	PP, SP	PP, **CI**	**PP**
	Hainan	CI, PP	CI, PP	CI, PP	CI, PP	CI, PP	CI, PP	CI, **PP**	**CI**
Southwest China	Chongqing	CP, PP	PP, CP	CI, CP	CI, CP	CI, CP	**CI, CP**	–	–
	Sichuan	CF, GF	GF, CF	GF, CF	**CF,** SP	SP, CI	CI, SP	**SP, GF**	–
	Guizhou	PP, CP	PP, CF	PP, CP	PP, CI	PP, CI	PP, CI	**CI, PP**	–
	Yunnan	NM, CI	CI, NM	CI, SP	CI, SP	CI, **SP**	CK, PP	CI, CP	**CI,** CP
	Tibet	CP, PP	CP, PP	CP, PP	CP, **PP**	CP	CP	CP	**CP**

CI: Chemical industry; CK: Coking plant; CP: Cement plant; CF: Ceramic factory; GF: Glass factory; NM: Non-ferrous metal smelting; PP: Power plant; SP: Steel plant; TH: Thermal production and supply.

Table 4
Provincial major stationary combustion source types in different CO HGI based on TF-IDF.

Region	Province	CO_HGI							
		≥5	≥6	≥7	≥8	≥9	≥10	≥11	= 12
North China	Beijing	PP, TH	NM, PP	PP	**PP**	–	–	–	–
	Tianjin	SP, PP	SP, CK	SP, CK	SP, CK	SP, **CK**	**SP**	–	–
	Hebei	SP, CK	SP, CK	SP, CK	SP, CK	SP, CK	SP, CK	SP, **CK**	**SP**
	Shanxi	CK, SP	CK, SP	CK, SP	CK, SP	SP, CK	CK, SP	SP, CI	**CK, SP**
	Inner Mongolia	SP, CK	SP, CK	SP, CK	SP, CK	SP, CK	SP, CK	**SP, CK**	–
Northeast China	Heilongjiang	TH, PP	TH, SP	SP, **TH**	SP, PP	**SP**	–	–	–
	Jilin	PP, SP	SP, PP	SP, PP	SP, PP	SP, PP	SP, PP	**PP, SP**	–
	Liaoning	SP, TH	SP, TH	SP, **TH**	SP, CK	SP, CK	SP, CK	SP, **CK**	**SP,** PP
Northwest China	Shaanxi	CI, TH	CP, TH	SP, CK	SP, CK	SP, CK	SP, CK	SP, CK	**SP, CK**
	Gansu	PP, SP	PP, SP	PP, SP	PP, CI	PP, SP	PP, SP	**PP,** SP	**SP,** CP
	Qinghai	NM, SP	SP, NM	SP, NM	SP, CP	SP, CP	SP, CP	SP, **CP**	**SP, NM**
	Ningxia	CI, CP	CI, PP	CI, CP	**CI,** PP	NM, **PP**	CK, CP	CK, CP	**CP, CK**
	Xinjiang	PP, CI	CI, PP	**PP,** NM	NM, **CI**	NM, SP	NM, SP	SP, NM	**SP, NM**
Central China	Henan	SP, NM	SP, NM	SP, NM	SP, **NM**	SP, CK	SP, CP	SP	**SP**
	Hubei	PP, SP	SP, NM	SP, PP	SP, PP	SP, PP	SP, PP	**PP,** SP	**SP,** CK
	Hunan	PP, CI	SP, CI	CI, SP	SP, **CI**	CK, SP	CK, SP	**CK,** SP	**SP,** PP
East China	Shanghai	PP, NM	PP	**PP**	–	–	–	–	–
	Jiangsu	CI, SP	SP, CI	SP, PP	SP, CI	SP, CI	CI, SP	CI, SP	**CI, SP**
	Zhejiang	CI, PP	CP, PP	PP, CI	CI, PP	CI, PP	CI, PP	**CI, PP**	–
	Anhui	SP, NM	SP, CI	SP, CI	SP, PP	SP, PP	SP, PP	PP, SP	**PP, SP**
	Fujian	SP, PI	SP, NM	SP, NM	SP, NM	SP, NM	SP, NM	**NM, SP**	–
	Jiangxi	SP, PP	SP, CP	SP, CI	SP, CI	SP, PP	SP, PP	**SP, PP**	–
	Shandong	SP, CI	SP, CI	SP, PP	SP, PP	SP, NM	SP, NM	**NM, SP**	SP, CP
South China	Guangdong	CF, GF	CF, CP	CF, CP	CF, **CP**	SP, **CF**	**SP**	–	–
	Guangxi	PP, SP	PP, SP	PP, SP	SP, **PP**	SP, CI	SP	**SP**	–
	Hainan	CP, CI	CI, CP	–	–	–	–	–	–
Southwest China	Chongqing	PP, CI	PP, CI	CI, PP	CI, **PP**	CI, GF	CI	**CI**	–
	Sichuan	CF, PP	PP, CI	CI, SP	CI, CK	CI, SP	**CI,** SP	SP	**SP**
	Guizhou	NM, PP	NM, PP	NM, CP	SP, PP	SP, **NM**	**PP,** CP	–	–
	Yunnan	NM, SP	SP, CI	SP, CI	CI, NM	CI, SP	CI, SP	**SP,** CI	**CI**
	Tibet	–	–	–	–	–	–	–	–

CI: Chemical industry; CK: Coking plant; CP: Cement plant; CF: Ceramic factory; GF: Glass factory; NM: Non-ferrous metal smelting; PP: Power plant; SP: Steel plant; TH: Thermal production and supply.

to the shorter lifetime of NO_2 compared to CO, hotspot extraction for NO_2 was more effective, and CO hotspot extraction was more susceptible to topographical influences. It is noteworthy that the NO_2 and CO hotspot grids exhibited substantial overlap in the major pollution sources. We further found that pollution hotspots and their corresponding concentrations showed a strong correlation with MEIC emissions. R^2 between NO_2 concentration and emissions was 0.937 in provinces with small land area (Shanghai, Tianjin, and Beijing) and 0.654 in others, while for CO, they were 0.849 and 0.659, respectively.

The TF-IDF analysis indicated that Steel plant and Power plant were the primary sources of NO_2 hotspots in most provinces. In northern provinces, heating demand during winter made Thermal production and supply sector a major NO_x emitter. Additionally, Coking plant and Ceramic factory contributed significantly to NO_x emissions in northern and southern provinces, respectively. For CO, the Steel plant displayed the highest TF-IDF weights at HGI = 12, indicating its dominant role in CO emissions. Coking plant was a major CO pollution source in northern and northwestern China, while the Chemical industry contributed significantly in eastern and southwestern provinces. In mineral-rich provinces like Qinghai, Xinjiang, and Shandong, Non-ferrous metal smelting emerged as a major CO-emitting sector. The TF-IDF analysis identified key industry contributors but did not exclude other sources. Our results provide pollution hotspot information to support provincial pollution control efforts and offer an observational constraint on the spatial locations of NO_x and CO emission sources for emission inventories.

CRediT authorship contribution statement

Mingyu Zeng: Writing – original draft, Visualization, Methodology, Formal analysis, Data curation. **Minghui Tao:** Writing – review & editing, Funding acquisition, Conceptualization. **Rong Li:** Funding acquisition. **Pengfei Ma:** Software. **Lijuan Zhang:** Investigation. **Jun Wang:** Supervision. **Lunche Wang:** Data curation. **Yi Wang:** Validation. **Haijun Huang:** Resources. **Liangfu Chen:** Project administration.

Declaration of competing interest

The authors declare that they have no known competing financial interests or personal relationships that could have appeared to influence the work reported in this paper.

Acknowledgments

This study was supported by National Natural Science Foundation of China (Grant No.42271382 and 42171354). Jun Wang's participation is made possible via the in-kind support (Lichtenberger Chair professorship) from University of Iowa. We thank European Space Agency (ESA) and the Netherlands Space Office (NSO) for providing TROPOMI products.

Appendix A. Supplementary data

Supplementary data to this article can be found online at https://doi.org/10.1016/j.atmosenv.2025.121176.

Data availability

Data will be made available on request.

References

Beirle, S., Boersma, K.F., Platt, U., Lawrence, M.G., Wagner, T., 2011. Megacity emissions and lifetimes of nitrogen oxides probed from space. Science 333 (6050), 1737–1739.

Beel, J., Gipp, B., Langer, S., Breitinger, C., 2016. Paper recommender systems: a literature survey. Int. J. Digit. Libr. 17, 305–338.
Bhanarkar, A.D., Goyal, S.K., Sivacoumar, R., Chalapati Rao, C.V., 2005. Assessment of contribution of SO_2 and NO_2 from different sources in Jamshedpur region, India. Atmos. Environ. 39 (40), 7745–7760.
Borsdorff, T., aan de Brugh, J., Hu, H., Hasekamp, O., Sussmann, R., Rettinger, M., Hase, F., Gross, J., Schneider, M., Garcia, O., Stremme, W., Grutter, M., Feist, D.G., Arnold, S.G., De Mazière, M., Kumar Sha, M., Pollard, D.F., Kiel, M., Roehl, C., et al., 2018. Mapping carbon monoxide pollution from space down to city scales with daily global coverage. Atmos. Meas. Tech. 11 (10), 5507–5518.
Chen, F., Knight, Q., Yang, Y.P., Shen, W., Zhao, C., 2012. Research on urban air quality evaluation method based on fractal model. China Environ. Sci. 32 (5), 954–960.
Chen, F., Wang, Q., Lai, Q., Wang, C.T., Ma, P.F., Zhou, Chunyan, Mao, H.Q., 2018. Research on remote sensing screening method for atmospheric environmental hotspot grid. China Environ. Sci. 38 (7), 2461–2470.
Cheng, Z., Li, L., Liu, J., 2018. Industrial structure, technical progress and carbon intensity in China's provinces. Renew. Sustain. Energy Rev. 81, 2935–2946.
Chen, B., Hu, J., Song, Z., Zhou, X., Zhao, L., Wang, Y., Chen, R., Ren, Y., 2023. Exploring high-resolution near-surface CO concentrations based on Himawari-8 top-of-atmosphere radiation data: assessing the distribution of city-level CO hotspots in China. Atmos. Environ. 312, 120021.
Crippa, M., Guizzardi, D., Muntean, M., Schaaf, E., Dentener, F., van Aardenne, J.A., Monni, S., Doering, U., Olivier, J.G.J., Pagliari, V., Janssens-Maenhout, G., 2018. Gridded emissions of air pollutants for the period 1970–2012 within EDGAR v4.3.2. Earth Syst. Sci. Data 10 (4), 1987–2013.
Deng, X., Tie, X., Zhou, X., Wu, D., Zhong, L., Tan, H., Li, F., Huang, X., Bi, X., Deng, T., 2008. Effects of Southeast Asia biomass burning on aerosols and ozone concentrations over the Pearl River Delta (PRD) region. Atmos. Environ. 42 (36), 8493–8501.
Daniel, J.S., Solomon, S., 1998. On the climate forcing of carbon monoxide. J. Geophys. Res. Atmos. 103 (D11), 13249–13260.
Duncan, B.N., Prados, A.I., Lamsal, L.N., Liu, Y., Streets, D.G., Gupta, P., Hilsenrath, E., Kahn, R.A., Nielsen, J.E., Beyersdorf, A.J., Burton, S.P., Fiore, A.M., Fishman, J., Henze, D.K., Hostetler, C.A., Krotkov, N.A., Lee, P., Lin, M., Pawson, S., et al., 2014. Satellite data of atmospheric pollution for U.S. air quality applications: examples of applications, summary of data end-user resources, answers to FAQs, and common mistakes to avoid. Atmos. Environ. 94, 647–662.
Finch, D.P., Palmer, P.I., Zhang, T., 2022. Automated detection of atmospheric NO_2 plumes from satellite data: a tool to help infer anthropogenic combustion emissions. Atmos. Meas. Tech. 15 (3), 721–733.
Fu, J., Tang, D., Grieneisen, M.L., Yang, F., Yang, J., Wu, G., Wang, C., Zhan, Y., 2023. A machine learning-based approach for fusing measurements from standard sites, low-cost sensors, and satellite retrievals: application to NO_2 pollution hotspot identification. Atmos. Environ. 302, 119756.
Geng, G., Liu, Y., Liu, Y., Liu, S., Cheng, J., Yan, L., Wu, N., Hu, H., Tong, D., Zheng, B., Yin, Z., He, K., Zhang, Q., 2024. Efficacy of China's clean air actions to tackle PM2.5 pollution between 2013 and 2020. Nat. Geosci. 17 (10), 987–994.
Haralick, R.M., Shapiro, L.G., 1985. Image segmentation techniques. Comput. Vis. Graph Image Process 29 (1), 100–132.
Hoesly, R.M., Smith, S.J., Feng, L., Klimont, Z., Janssens-Maenhout, G., Pitkanen, T., Seibert, J.J., Vu, L., Andres, R.J., Bolt, R.M., Bond, T.C., Dawidowski, L., Kholod, N., Kurokawa, J., Li, M., Liu, L., Lu, Z., Moura, M.C.P., O'Rourke, P.R., Zhang, Q., 2018. Historical (1750–2014) anthropogenic emissions of reactive gases and aerosols from the Community Emissions Data System (CEDS). Geosci. Model Dev. (GMD) 11 (1), 369–408.
Hogue, S., Marland, E., Andres, R.J., Marland, G., Woodard, D., 2016. Uncertainty in gridded CO_2 emissions estimates. Earths Future 4 (5), 225–239.
Holloway, T., Levy, H., Kasibhatla, P., 2000. Global distribution of carbon monoxide. J. Geophys. Res. Atmos. 105 (D10), 12123–12147.
Huang, K., Fu, J.S., Hsu, N.C., Gao, Y., Dong, X., Tsay, S.C., Lam, Y.F., 2013. Impact assessment of biomass burning on air quality in Southeast and East Asia during BASE-ASIA. Atmos. Environ. 78, 291–302.
Jamali, S., Klingmyr, D., Tagesson, T., 2020. Global-scale patterns and trends in tropospheric NO_2 concentrations, 2005–2018. Remote Sens. 12 (21), 3526.
Jion, Most M.M. F., Jannat, J.N., Mia, Md Y., Ali, Md A., Islam, Md S., Ibrahim, S.M., Pal, S.C., Islam, A., Sarker, A., Malafaia, G., Bilal, M., Islam, A.R.M.T., 2023. A critical review and prospect of NO_2 and SO_2 pollution over Asia: hotspots, trends, and sources. Sci. Total Environ. 876, 162851.
Kong, H., Lin, J., Zhang, Y., Li, C., Xu, C., Shen, L., Liu, X., Yang, K., Su, H., Xu, W., 2023. High natural nitric oxide emissions from lakes on Tibetan Plateau under rapid warming. Nat. Geosci. 16 (6), 474–477.
Li, M., Liu, H., Geng, G., Hong, C., Liu, F., Song, Y., Tong, D., Zheng, B., Cui, H., Man, H., Zhang, Q., He, K., 2017. Anthropogenic emission inventories in China: a review. Natl. Sci. Rev. 4 (6), 834–866.
Martin, R.V., 2008. Satellite remote sensing of surface air quality. Atmos. Environ. 42 (34), 7823–7843.
Nguyen, E., 2013. Text mining and network analysis of digital libraries in R. Data Mining Applications with R, pp. 95–115.
Pani, S.K., Ou-Yang, C.-F., Wang, S.-H., Ogren, J.A., Sheridan, P.J., Sheu, G.-R., Lin, N.-H., 2019. Relationship between long-range transported atmospheric black carbon and carbon monoxide at a high-altitude background station in East Asia. Atmos. Environ. 210, 86–99.
Pommier, M., McLinden, C.A., Deeter, M., 2013. Relative changes in CO emissions over megacities based on observations from space. Geophys. Res. Lett. 40 (14), 3766–3771.
Pommier, M., 2023. Estimations of NO_x emissions, NO_2 lifetime and their temporal variation over three British urbanised regions in 2019 using TROPOMI NO_2 observations. Environ. Scie. Atmos. 3 (2), 408–421.
Richter, A., Burrows, J.P., Nüß, H., Granier, C., Niemeier, U., 2005. Increase in tropospheric nitrogen dioxide over China observed from space. Nature 437 (7055), 129–132.
Salton, G., Buckley, C., 1988. Term-weighting approaches in automatic text retrieval. Inf. Process. Manag. 24 (5), 513–523.
Schuit, B.J., Maasakkers, J.D., Bijl, P., Mahapatra, G., van den Berg, A.-W., Pandey, S., Lorente, A., Borsdorff, T., Houweling, S., Varon, D.J., McKeever, J., Jervis, D., Girard, M., Irakulis-Loitxate, I., Gorroño, J., Guanter, L., Cusworth, D.H., Aben, I., 2023. Automated detection and monitoring of methane super-emitters using satellite data. Atmos. Chem. Phys. 23 (16), 9071–9098.
Sezgin, M., Sankur, B.L., 2004. Survey over image thresholding techniques and quantitative performance evaluation. J. Electron. Imag. 13 (1), 146–168.
Shen, W., 2011. Fractal invariable distribution and its application in large-sized and super large-sized mineral deposits. Geosci. Front. 2 (1), 87–91.
Sheng, H., Fan, L., Chen, M., Wang, H., Huang, H., Ye, D., 2024. Identification of NO_x emissions and source characteristics by TROPOMI observations–A case study in north-central Henan, China. Sci. Total Environ. 931, 172779.
Sun, K., Zhu, L., Cady-Pereira, K., Chan Miller, C., Chance, K., Clarisse, L., Coheur, P.-F., González Abad, G., Huang, G., Liu, X., Van Damme, M., Yang, K., Zondlo, M., 2018. A physics-based approach to oversample multi-satellite, multispecies observations to a common grid. Atmos. Meas. Tech. 11 (12), 6679–6701.
Tian, Y., Liu, C., Sun, Y., Borsdorff, T., Landgraf, J., Lu, X., Palm, M., Notholt, J., 2022. Satellite observations reveal a large CO emission discrepancy from industrial point sources over China. Geophys. Res. Lett. 49 (5), e2021GL097312.
van Geffen, J., Boersma, K.F., Eskes, H., Sneep, M., ter Linden, M., Zara, M., Veefkind, J. P., 2020. S5P TROPOMI NO_2 slant column retrieval: method, stability, uncertainties and comparisons with OMI. Atmos. Meas. Tech. 13 (3), 1315–1335.
Varon, D.J., Jervis, D., Pandey, S., Gallardo, S.L., Balasus, N., Yang, L.H., Jacob, D.J., 2024. Quantifying NO_x point sources with Landsat and Sentinel-2 satellite observations of NO_2 plumes. Proc. Natl. Acad. Sci. USA 121 (27), e2317077121.
Wang, K., Wu, K., Wang, C., Tong, Y., Gao, J., Zuo, P., Zhang, X., Yue, T., 2022. Identification of NO_x hotspots from oversampled TROPOMI NO_2 column based on image segmentation method. Sci. Total Environ. 803, 150007.
Wang, Y., Ali, M.A., Bilal, M., Qiu, Z., Mhawish, A., Almazroui, M., Shahid, S., Islam, M. N., Zhang, Y., Haque, M.N., 2021. Identification of NO_2 and SO_2 pollution hotspots and sources in Jiangsu province of China. Remote Sens. 13 (18). Article 18.
Xue, R., Wang, S., Zhang, S., He, S., Liu, J., Tanvir, A., Zhou, B., 2022. Estimating city NO_x emissions from TROPOMI high spatial resolution observations–A case study on Yangtze River Delta, China. Urban Clim. 43, 101150.
Yin, X., Kang, S., Rupakheti, M., De Foy, B., Li, P., Yang, J., Wu, K., Zhang, Q., Rupakheti, D., 2021. Influence of transboundary air pollution on air quality in southwestern China. Geosci. Front. 12 (6), 101239.